Nano-Antenna Arrays for the Infrared Regime

Gergo P. Szakmany[1] Alexei O. Orlov[1] Gary H. Bernstein[1] Wolfgang Porod[1]
Mario Bareiss[2] Paolo Lugli[2] Johannes A. Russer[2] Christian Jirauschek[2] Peter Russer[2]
Michel T. Ivrlač[3] Josef A. Nossek[3]

[1]Center for Nano Science and Technology
Department of Electrical Engineering
University of Notre Dame
Notre Dame, IN, U.S.A
email: {gszakman, aorlov, bernstein.1, porod}@nd.edu

[2]Institute for Nanoelectronics
Technische Universität München
Munich, Germany
email: {bareiss, lugli, jrusser, jirauschek, russer}@tum.de

[3]Institute for Circuit Theory and Signal Processing
Technische Universität München
Munich, Germany
email: {ivrlac, josef.a.nossek}@tum.de

***Abstract*—Infrared detectors for the long-wave infrared range (LWIR) are of special interest due to their ability to detect blackbody radiation of objects at room temperature. Such detectors are attractive candidates for various applications including energy harvesting, target tracking, and thermal imaging, but their applications to communication systems have been largely unexplored. In this paper, we combine our previous work on antenna-coupled thermocouples with a new approach to near-field-coupled nano-antennas, which might open up the possibility of obtaining carrier phase after envelope demodulation.**

I. Introduction

Infrared (IR) detectors for the long-wave infrared (LWIR) regime are of special interest because of their ability to detect blackbody radiation of objects at room temperature. Such detectors are attractive candidates for various applications including energy harvesting [1], target tracking [2], and thermal imaging [3], but their applications to communication systems have been largely unexplored. The on-chip integration of antennas opens new vistas for novel devices and integrated systems for all those known and potential applications [4].

In this paper, we combine our previous work on antenna-coupled thermocouples with some new approach to near-field-coupled nano-antennas, which might open the possibility of obtaining carrier phase after envelope demodulation. Antenna-coupled nanowire thermocouples are constructed form an antenna receiving the IR radiation, and from a thermocouple (TC) converting the thermal energy to electrical signals. TCs are constructed from two conductors with different absolute Seebeck coefficients (S_A and S_B), configured to form two junctions, commonly referred to as the hot and cold junctions. A temperature difference (ΔT) between the hot and cold junctions leads to a measurable open-circuit voltage (u_{OC}) due to the Seebeck effect as expressed by

$$u_{\mathrm{OC}} = \Delta T \left(S_A - S_B \right), \tag{1}$$

where $(S_A - S_B)$ is the relative Seebeck coefficient.

We use a dipole antenna as the receiving element in our antenna-coupled nanowire thermocouples. At resonance, the radiation-induced antenna currents exhibit a maximum at the center of the dipole antenna, which, due to Joule heating, functions as the hot junction of the TC. The open-circuit voltage of the TC IR-detector is proportional to the temperature difference between the hot and cold junctions, and to the relative Seebeck coefficients according to (1). Therefore, the location of the TC hot junction is engineered at the center of the IR antenna to maximize the temperature difference between the two junctions. Figure 1(a) shows a schematic of our IR detector.

Large-scale fabrication of antenna-coupled infrared detectors is possible using a novel nanotransfer-printing (NTP) process [5]. As shown in [6], nearly 1 million devices were placed on a small chip, and the response of several sub-assemblies to LWIR radiation was measured. This technology opens up the possibilities to fabricate large arrays of antenna-coupled detectors at low-cost, virtually on any substrate, especially by exploiting the reduction of the absolute Seebeck coefficient based on geometrical effects [7].

II. Design and Fabrication

A. Antenna Design and Substrate Engineering

The geometry of the antenna determines the resonant frequency [8], the directivity [9], and the polarization [10] of the detector. In previous work, we built bow tie [11] and dipole [12] antenna-coupled nanowire thermocouples. In this work, we present dipole antennas. They are polarization dependent, and their antenna length determines the operation frequency. For 10.6 µm IR radiation, the resonant dipole length was calculated by COMSOL Multiphysics® simulations, and found to be 2.4 µm. The directivity of the devices was increased by fabricating the antennas on top of a ground plane layer separated by a 1.2 µm thick quarter-wave dielectric layer. This ensures a constructive interference at the antenna between the incident and the reflected waves from the ground plane.

B. Fabrication

The substrate of our devices is a 625 µm thick Si-wafer that is coated with 100 nm of Al and 1.2 µm PECVD-deposited SiO_2.

ISBN 978-3-8007-3584-6

While the Al serves as the ground plane, the SiO_2 layer ensures electrical isolation between the devices and serves as a quarter-wave-matching layer.

The fabrication of the antenna-coupled nanowire TCs involved optical and electron beam lithography (EBL). Bonding pads for electrical and optical measurements were patterned by optical lithography and metalized by 200 nm thick Au using 10 nm thick Ti as an adhesion layer. The dipole antenna and the first half of the TC (»metal A«) were exposed by EBL and metalized by 45 nm thick Pd. During the second EBL step, the

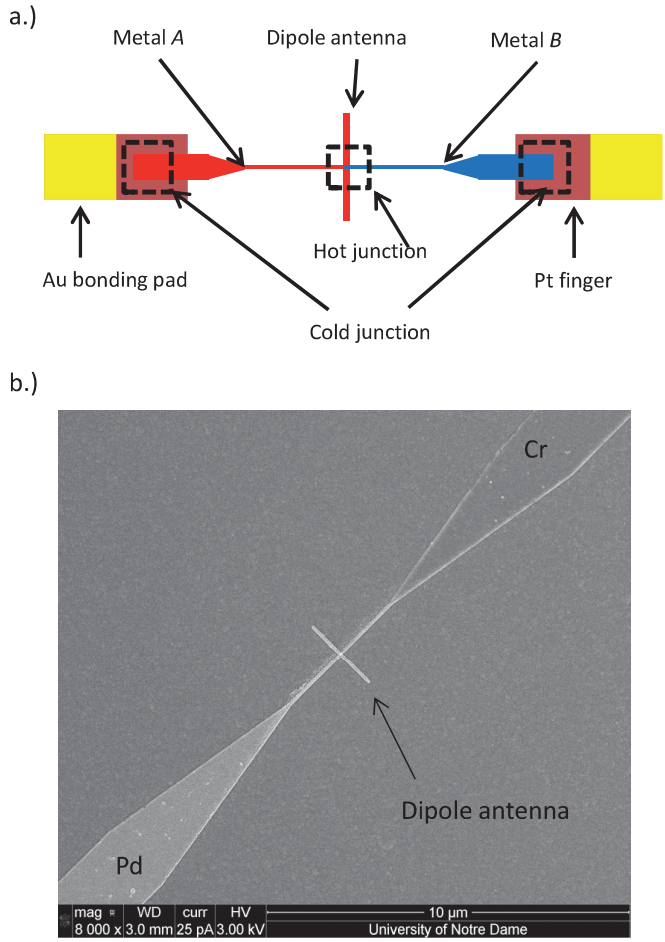

Figure 1: The schematic diagram (a) of the antenna-coupled nanowire thermocouple shows the location of the hot and cold junction of the IR detector. The hot junction is formed at the center of the antenna, where metals A and B overlap. The cold junctions are located several microns away, where the metals A and B overlap with the Au bonding pads. In part (b), one can see a scanning electron microscope image of a Cr/Pd antenna-coupled nanowire thermocouple. The dipole antenna and one part of the thermocouple are made from Pd, the other part of the thermocouple being made from Cr.

second half of the TC (»metal B«) was patterned and metalized by 45 nm thick electron beam evaporated Cr. The hot junction of the TCs is located at the center of the antenna, where the Cr and Pd wires overlap with a 75×75 nm^2 large junction area.

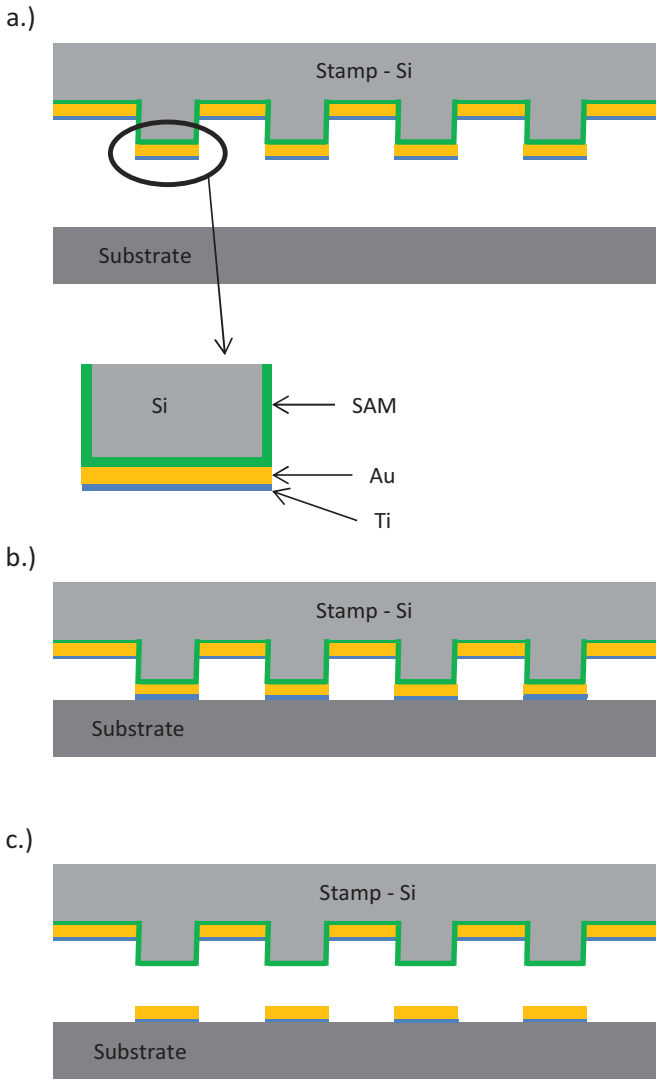

Figure 2: Schematic of the NTP fabrication steps. (a.) The Si stamp carries the pattern and has got the metals (Au, Ti) in reverse order compare to the target device. (b.) The stamp and the target substrate are in physical contact. (c.) The Au and Ti layers are transferred to the substrate creating our intended device. The SAM remains on the stamp for possible further repetition of the process.

The dipole antenna and its thin lead lines are 75 nm wide. A fabricated device is shown in Figure 1.

In addition to the lithographic process which was described above, large arrays of antenna-coupled IR detectors were fabricated by NTP, which is a fast and cost effective fabrication method and does not require any lithographic process steps. The NTP process involves a stamp with the desired geometry, and »inked« with the metal layers of the devices. It is mechanically pressed against the substrate for pattern transfer.

The adhesive surface of the Si stamp first is coated by a self-assembled monolayer (SAM) to facilitate the metal transfer from the stamp to the substrate. Then, the material of the

ISBN 978-3-8007-3584-6

devices is deposited on the stamp, followed by a thin adhesion promoter, such as Ti. When the stamp is brought into contact with the Si or glass target substrate, the hydrophilic Ti layer binds to the hydrophilic substrate and the metal layers are transferred onto the substrate. Figure 2 schematically shows the steps of the NTP fabrication process. Figure 3 shows a scanning electron microscope (SEM) image of a fabricated antenna array.

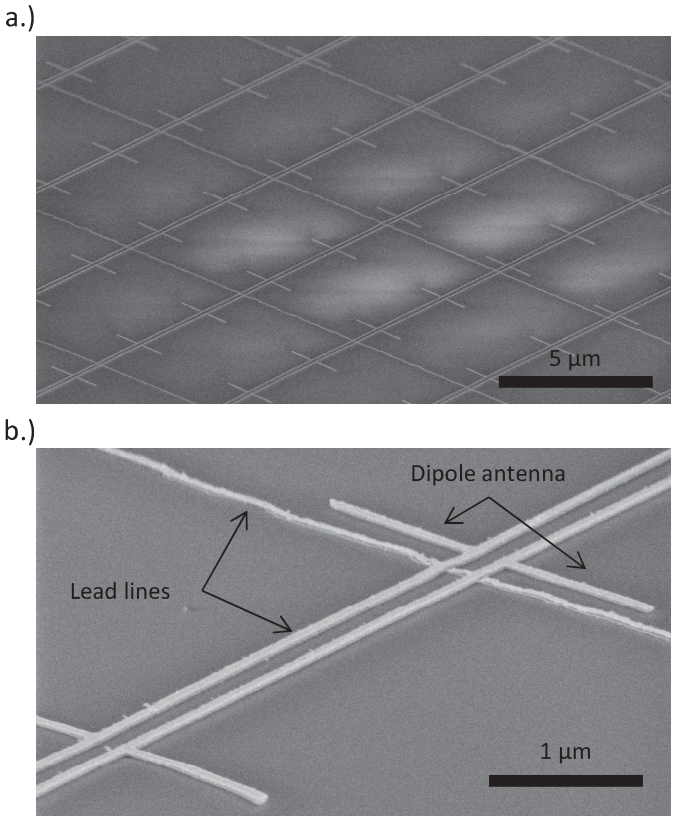

Figure 3: Scanning electron micrographs of the nanoantennas. (a) A Section of a nano-antenna array fabricated with NTP. (b) Enlarged view of an antenna and its lead lines. The width of the leadlines and the antenna is 100 nm, and the length of the dipole antenna is 2.1 µm. The thickness of the metals is 45 nm.

III. Measurements & Results

A. Infrared Measurement

An infrared illumination of the antenna-coupled infrared detectors was carried out with a CO_2 laser. The devices were illuminated by a 1.42 W/cm^2 intensity, linearly polarized laser beam. The beam was square wave modulated by a mechanical chopper at 1 kHz. The open-circuit voltage response of the detectors was measured by a low-noise differential-voltage amplifier and a lock-in amplifier that was synchronized with the chopping frequency. The polarization angle between the laser beam and the axis of the dipole antenna was set by a half-wave plate.

The polarization dependent response of the device under test was measured during a constant, 0.1 deg/s, rotation of the half-wave plate. Maximum antenna response was measured when the polarization of the electric field was parallel with the antenna axis. Minimum response was measured, when the antenna axis and the polarization of the laser beam were perpendicular to each other. Figure 4 shows a typical polarization dependent response of a Cr/Pd antenna-coupled thermocouple, which can be seen to exhibit the cosine-squared dependence predicted by classical antenna theory [13].

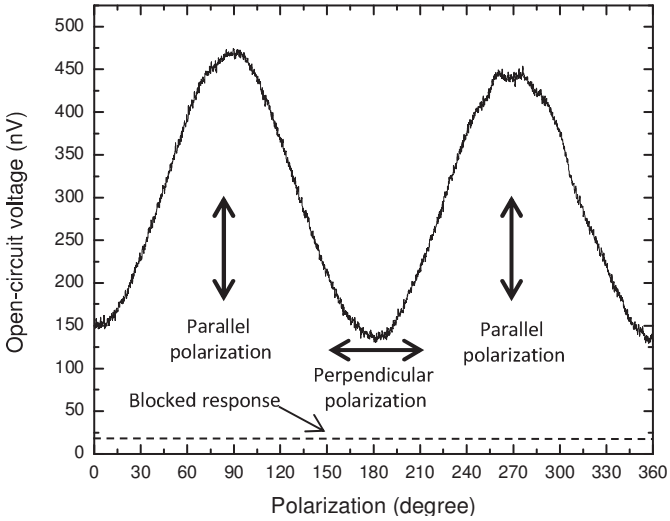

Figure 4: Polarization dependent response of a Cr/Pd antenna-coupled nanowire thermocouple. Maximum response was measured when the antenna axis and the polarization of the laser beam was parallel (90 deg and 270 deg), and minimum when they were perpendicular to each other (0 deg, 180 deg, and 360 deg).

The blocked response, i.e., when the IR detector was not illuminated, is only 3.7% of the maximum response, which is equal to the noise voltage of the detector. The perpendicular response was seven times larger than the blocked response. This is due to the fact that since the length of the lead lines of the dipole antenna is comparable to the resonant antenna length, the lead lines also act as antennas. At the perpendicular state, they are responsible for the hot junction heating and for the resulting difference between the measured blocked and perpendicular open-circuit voltage.

B. Substrate Heating Effect of the Laser Beam

The temperature increase of the silicon substrate caused by the infrared heating of the laser beam was measured with a resistive temperature device (RTD) co-located on the chip by the antennas. A four-terminal, or Kelvin, connection method, was used to measure the change of resistance of a 3 µm long wire segment shown in Figure 5. A small, 1 µA test current was flown between the two outside terminals (I^+ and I^-) of the thermometer. Therefore, the dissipated power by the thermometer is less than 0.3 nW, inducing a negligible self-heating. The voltage drop across the thermometer was measured between two inside terminals (V^+ and V^-). Since the current is

ISBN 978-3-8007-3584-6

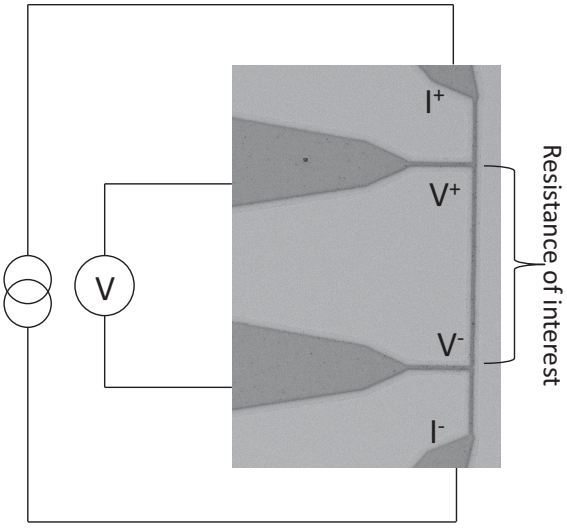

Figure 5: Resistive temperature device to measure the substrate heating by the IR radiation. A constant current is let flown between the two outer terminals (I^+ and I^-), and the voltage drop is measured between the two inner terminals (V^+ and V^-). The temperature change of the wire segment between V^+ and V^- is calculated from the resistance change [7].

known and the voltage drop was measured, the resistance of the thermometer was calculated from Ohm's law [7].

The resistance change of a metal as a function of temperature is defined by the temperature coefficient of the resistance (TCR) and expressed as

$$\alpha(T_0) = \frac{1}{R(T_0)}\frac{\mathrm{d}R}{\mathrm{d}T}, \qquad (2)$$

where T_0 is the initial temperature, $\mathrm{d}R$ is the resistance change, $\mathrm{d}T$ is the temperature change, and $R(T_0)$ is the resistance at the temperature T_0.

The TCR of metals is reduced in thin-films and nanowires when compared to the bulk materials [14], [15]. The TCR of the Pd thermometers was determined by calibrating them in a cryostat to a reference integrated circuit temperature transducer (AD590), which was placed in close proximity to the chip to measure the ambient temperature. The resistance at various temperatures, ranging from 240 K to 290 K, was measured using a resistance bridge (Picowatt AVS-47A). The resistance changed linearly as a function of temperature within the measured temperature range. The TCR of Pd thermometers was calculated at 290 K using (2), and found to be 0.199 %/K.

The calibrated thermometer was connected to a low-noise differential-voltage amplifier and a lock-in amplifier to measure its resistance change as the incident laser beam heated up the substrate. The result is shown in Figure 6. At the beginning (laser OFF), the incident laser beam was blocked and the chip was in thermal equilibrium with the ambient temperature. Later (laser ON), the entire chip was illuminated by the laser beam with 1.42 W/cm^2 intensity. The substrate temperature

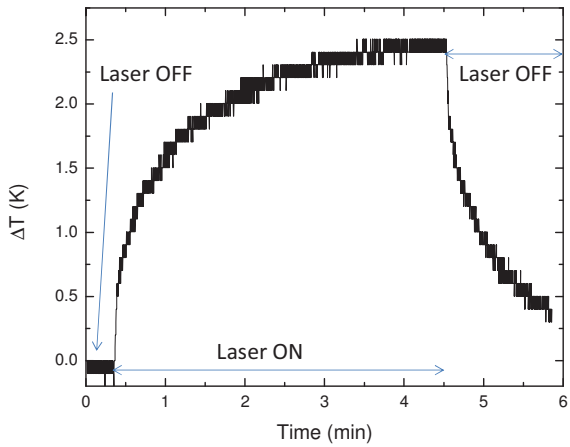

Figure 6: Temperature increase of the substrate as a function of time due to the heating by the laser beam. The antenna-coupled nanowire thermocouples resolve few mK of temperature difference due to the polarized beam, in a large, 2.5 K background temperature change [7].

was increased due to the heating effect of the laser beam. After 4 minutes, the temperature increase saturated. The measured background temperature increase was 2.5 K, generated by the infrared heating of the laser. Finally (laser OFF), the laser beam was blocked again, so that the chip was not illuminated any more and the substrate began cooling down [7].

The diameter of the laser beam was 4 mm as measured by a so-called knife-edge measurement. Because of the large beam footprint, the laser beam heated up the entire chip. The temperature of the hot and cold junction rose equally, since both of them fall into the peak radiation of the beam. Therefore, the measured open circuit voltage of the antenna-coupled thermocouple was clearly the difference between the hot and cold junction induced by the dissipated antenna current.

Our antenna-coupled thermocouples were able to detect a temperature increase as small as tens of a mK, even in a presence of a large, 2.5 K background temperature variation.

C. Printed Antenna Arrays

Infrared response of the antenna arrays were measured similarly. It showed a cosine-squared polarization-dependent response confirming that their response is caused by the radiation induced antenna currents.

These experiments confirm that antenna-coupled nanowire thermocouples are capable of detecting very small, few mK, temperature differences. A large number of such nano-antenna structures can, at least in principle, be placed sufficiently close to each other, such that they experience the near field of the neighbor. While this principle is well established, we have not yet demonstrated it in experiment for our antenna-coupled thermocouples. Nevertheless, this possibility opens the door for some intriguing possibilities, as described below.

ISBN 978-3-8007-3584-6

IV. Thermoelectric Detection

A. The Seebeck Effect

All observations support a thermoelectric detection mechanism, that is, a hot junction resulting from heating caused by radiation-induced antenna currents.

In bulk solids the linear transport equations for charge and heat can be summarized in

$$\boldsymbol{E} = \boldsymbol{\rho}\boldsymbol{J} + \boldsymbol{S}\nabla T\,, \tag{3a}$$

$$\boldsymbol{Q} = \boldsymbol{\pi}\boldsymbol{J} - \boldsymbol{\kappa}\nabla T\,, \tag{3b}$$

where $\boldsymbol{E}$ is the electric field vector, $\boldsymbol{J}$ is the electric current density, T is the temperature, $\boldsymbol{Q}$ is the heat flux density, and $\boldsymbol{\rho}$, $\boldsymbol{S}$, $\boldsymbol{\pi}$, and $\boldsymbol{\kappa}$ are the resistivity-, Seebeck-, Peltier- and thermal conductivity tensors, respectively [16, p. 195], [17].

The radio-frequency (RF) electric field accelerates the electrons in the electron gas of the thermocouple metals. The Joule heating of the thermocouple occurs through the interaction of the electrons with the lattice vibrations of the metal and in case of thin metallic layers also with the lattice vibrations of the substrate [18], [19]. However, for the Seebeck effect the elevation of the electron temperature is relevant.

When the thermocouple dimensions are considerably larger than the electron-electron relaxation length, the electrons are distributed according to the Fermi-Dirac statistics. From (3a) we obtain for $\boldsymbol{J} = \boldsymbol{0}$, assuming a scalar Seebeck coefficient S the relation

$$\nabla u_S = -S\,\nabla T\,. \tag{4}$$

For the case of metals, the Seebeck coefficient is given by the Mott relation, [20], [21]

$$S = \frac{\pi^2}{3}\left(\frac{k_B^2 T}{e_0}\right)\left(\frac{\partial \ln(\sigma(E_{el}))}{\partial E_{el}}\right), \tag{5}$$

where σ is the electrical conductivity, E_{el} the electron energy, k_B the Boltzmann constant and e_0 is the elementary charge.

If a mesoscopic thermocouple on the basis of the Seebeck effect with dimensions in the order of some ten nanometers, or so, is used, the electron temperature should be raised over distances the same order of magnitude. This makes it reasonable to collect the incident radiation with an antenna and to concentrate the electron heating in a small volume. The dissipated radiation will first raise the electron temperature. The thermal energy will be passed over to the lattice, and, finally to the environment via heat conduction and/or radiation.

The coaction of the mesoscopic Seebeck coefficient and interfacial thermal conductance in coherent electron and heat transport through a point-like contact produces an atomic Seebeck effect [22].

We note in passing, that experiments clearly show that, different from the ordinary Seebeck effect, the thermo voltage is also generated when the material of the thermocouples is identical on both sides. Discussion of whether mesoscopic effects may yield a geometry dependent Seebeck effect is, however, beyond the scope of this paper.

B. Thermal Conduction in the Thermocouple Substrate

Figure 7 shows the cross sectional view through a substrate of thickness d with a circular metallic patch of radius r_0. In the following, we will investigate the thermal pulse response of the substrate region under the patch for an impulsive heating of the patch.

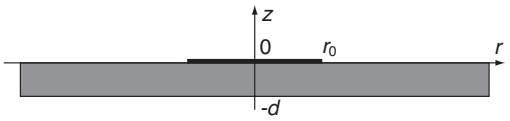

Figure 7: Cross sectional view through the disk with heated patch.

Consider the partial differential equation describing the heat conduction in the cylindrical coordinate system r, ϕ, z,

$$\frac{\partial^2 T}{\partial r^2} + \frac{1}{r}\frac{\partial T}{\partial r} + \frac{1}{r^2}\frac{\partial^2 T}{\partial \phi^2} + \frac{\partial^2 T}{\partial z^2} = \frac{1}{\alpha}\frac{\partial T}{\partial t}\,, \tag{6}$$

where t is the time, $T(r, \phi, z, t)$ is the temperature and α is the thermal diffusivity given by

$$\alpha = \frac{k}{\rho c_p}\,, \tag{7}$$

where k is the thermal conductivity, while ρ is the density and c_p is the specific heat of the material [23]. Bulk silicon has the approximate thermal conductivity of $\kappa = 148\,\mathrm{Wm^{-1}K^{-1}}$ [18], the room temperature density $\rho = 2329\,\mathrm{kg\,m^{-3}}$, and the specific heat $c_p = 700\,\mathrm{J\,kg^{-1}K^{-1}}$ [24]. With (7) this yields an approximate thermal diffusivity $\alpha = 9.078 \times 10^{-5}\,\mathrm{m^2 s^{-1}}$.

Consider a disk of thickness d and assume $z \in [-d, 0]$. In this case we can expand $T(r, z, t)$ in z direction into a Fourier series and obtain

$$T(r, z, t) = \sum_{n=-\infty}^{\infty} \int_0^{\infty} C_n(\beta)\, e^{\frac{2\pi j n z}{d}} J_n(\beta r)\, e^{-\alpha\left(\beta^2 + \left(\frac{2\pi n}{d}\right)^2\right)t} d\beta\,, \tag{8}$$

where β denotes the radial phase coefficient of the heat diffusion wave. The partial wave with the radial wave coefficient β and the vertical wave index n decays with a time constant

$$\tau_n(\beta) = \frac{1}{\alpha\left[\beta^2 + \left(\frac{2\pi n}{d}\right)^2\right]}\,. \tag{9}$$

To give a rough estimate of the time constant for the decay of the local heating under the patch with radius r_0 in Figure 7 we consider the partial wave with $n = 0$ where the radial part $J_0(\beta r)$ exhibits its first zero at $r = r_0$, i.e. for $\beta = 2.405\, r_0^{-1}$. The time constant computed from (9) on the basis of this assumption is proportional to r_0^2. For $r_0 = 25\,\mathrm{nm}$, we obtain a time constant of 1.19 ps and for $r_0 = 10\,\mathrm{nm}$ a time constant of 0.19 ps. This demonstrates that a mesoscopic thermocouple is an *extremely fast* square-law detector.

For the exact solution of the initial value problem of (6) we have to compute the $C_n(\beta)$ from the initial temperature distribution

$$T(r, z, 0) = \sum_{n=-\infty}^{\infty} \int_0^{\infty} C_n(\beta)\, e^{\frac{2\pi j n z}{d}} J_n(\beta r)\, d\beta\,. \tag{10}$$

ISBN 978-3-8007-3584-6

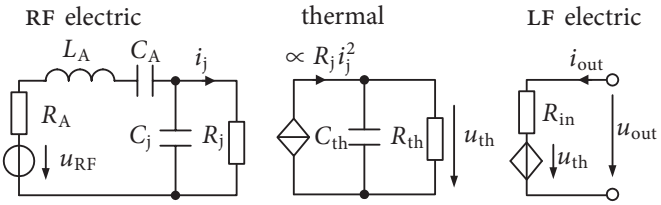

Figure 8: Equivalent circuit of antenna with thermocouple.

To compute the thermal pulse response for the disk shown in Figure 7 we assume that at time $t = 0$ the patch is impulsively heated such that the temperature under the patch is raised within an infinitely thin layer at $z = 0$ and uniformly in the region $0 \le r \le r_0$. So we choose the initial condition

$$T(r, z, 0) = \delta(z)\,\sigma(r_0 - r)\,. \tag{11}$$

From this the $C_n(\beta)$ can be computed by Fourier expansion for the z dependence and inverse Hankel transform for the radial dependence. A detailed analysis will be subject of a forthcoming paper.

We have to consider that the thermal analysis at dimensions in the nanometer scale deals with sub-continuum phenomena as ballistic electron transport since the structure dimensions are in the order or less than mean free paths of the electrons (5-10 nm) and the phonons (200-300 nm) in bulk silicon at room temperature [18]. Therefore, classical diffusion theory predictions in heat conduction may not be applicable.

C. The Equivalent Circuit of the Thermocouple

Lumped element circuit models of integrated antennas provide a compact functional description [25], [26]. In the Figure 8, the equivalent circuit of a thermocouple fed by a small antenna is shown. It consists of an electric RF part, a thermal part and an electric low frequency part. The open-circuit RF voltage, u_{RF}, of the antenna is given by

$$u_{RF}(t) = h_{eff} E_{inc}(t) \tag{12}$$

where E_{inc} denotes the tangential part of the incident electric RF field, and h_{eff} is the effective antenna length, while the combination of R_A, C_A and L_A constitute the antenna output impedance. The RF impedance of the thermocouple is characterized by the junction resistance R_j in parallel with the junction capacitance C_j.

The dissipated power, $R_j i_j^2$, is heating the junction and increases the junction temperature by ΔT. The thermal properties of the junction are characterized by the thermal capacitance C_{th} and the thermal resistance R_{th}.

The thermo voltage $u_{th}(t)$ is given by

$$u_{th}(t) = k \int_{-\infty}^{t} i_j^2(t) e^{-\frac{t-t_1}{\tau_{th}}} dt_1\,, \tag{13}$$

where τ_{th} is the thermal time constant. In the equivalent circuit, $u_{th}(t)$ is modeled by the controlled voltage source u_{th}. The thermal time constant can be modeled by R_{th} and C_{th} with $R_{th} C_{th} = \tau_{th}$.

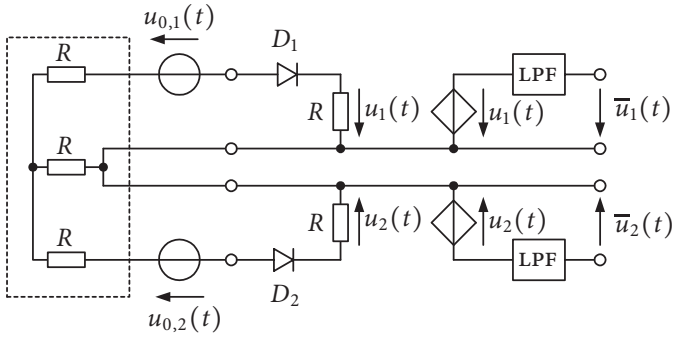

Figure 9: Two envelope demodulators connected to a simple twoport voltage generator with mutual coupling between its ports. To ease analysis, the low-pass filters are connected via buffer amplifiers.

This results in a thermo voltage $u_{th}(t)$, which, in turn, can be observed as the output voltage

$$u_{out}(t) = u_{th}(t) + R_{in} i_{out}(t), \tag{14}$$

where $i_{out}(t)$ is the load current associated with the observation of the thermal voltage. Note that all voltages and currents are real functions rather than complex envelopes.

V. Carrier Phase Recovery

Due to the signal detection by means of the Seebeck effect, the detected signal is a reaction to radiation induced antenna heating. Like in the case of other square-law detectors [27], e.g. semiconductor junction diodes, also in the case of the thermocouple detector no carrier phase information is obtainable from the detected signal. Apparently, the direction-dependent differences in carrier phases of the signals received by the antenna array cannot be used for the estimation of direction of arrival [28] or spatial processing [29]. This does not impair the extraction of receive array gain [30] and diversity gain [31], [32], for both can be obtained from simply adding up the demodulated signals. Spatial multiplexing [33], [34], however, requires that signals impinging from different directions can be distinguished. Having information about the carrier phases certainly would help a lot in this regard.

Interestingly, it might actually be possible to extract information about carrier phase from the demodulated signal, provided that: 1) the demodulation can act back on the sensors, and 2) the sensors experience mutual coupling. This last requirement can be easily fulfilled by placing the dipoles in close proximity (below half the wavelength) to their neighbors. The first requirement is more intriguing and needs further experimental and theoretical investigation.

In order to explain this idea consider an *envelope demodulator* [35] as shown in Figure 9, for the case of two sensors with mutual coupling. While it seems that envelope demodulation also suffers from the inability to obtain carrier phase information, we have the case that 1) the diodes act back on the sensors and 2) due to mutual coupling each sensor also senses the action of the other sensor's diode. Referring to the circuit

ISBN 978-3-8007-3584-6

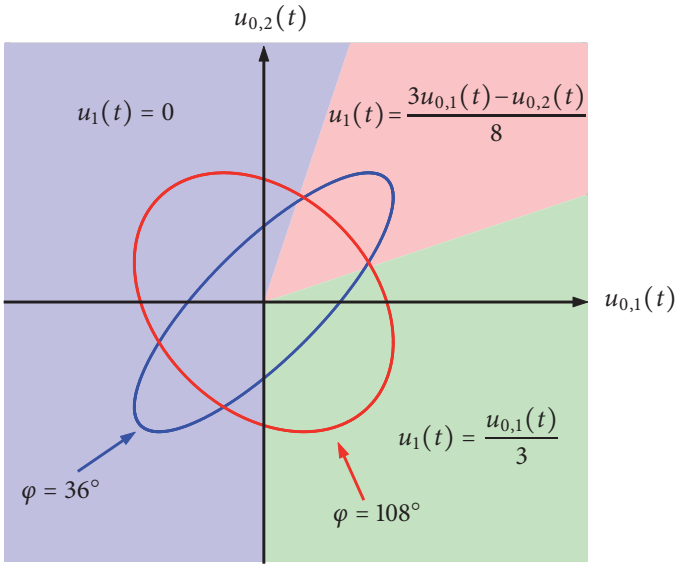

Figure 10: Visualization of the voltage $u_1(t)$ as it depends on $u_{0,1}(t)$ and $u_{0,2}(t)$. The set of pairs $(u_{0,1}(t), u_{0,2}(t))$ which correspond to two different phase differences are also shown.

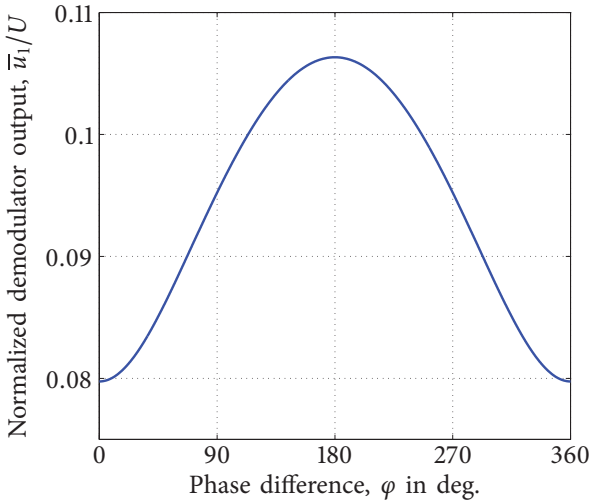

Figure 11: Output voltage, $\overline{u}_1$ of the low-pass filter as a fraction of the carrier amplitude, U, displayed as function of the phase difference, φ.

shown in Figure 9, the sensors are modeled by two voltages sources, $u_{0,1}(t)$ and $u_{0,2}(t)$, which are connected in series with a passive twoport that provides the mutual coupling. For sake of simplicity, the passive twoport consists of just three resistances, R. The rectification needed for the envelope demodulation is provided by the ideal diodes, D_1 and D_2. Now suppose that the open-circuit voltages of the twoport generator are given by:

$$u_{0,1}(t) = U\cos(\omega t), \quad u_{0,2}(t) = U\cos(\omega t + \varphi). \tag{15}$$

Both signals represent an unmodulated carrier and differ only in their phases by the amount φ. We will see in the following that information about φ is indeed available at the *output* of each low-pass filter (LPF). For ease of analysis, we let each LPF couple to the rectified voltage via a unity gain buffer. In this way, the non-linear part of the circuit is memoryless which greatly simplifies its analysis. Because the diodes are assumed ideal, it is clear that in order to have $u_1(t) \neq 0$, it is necessary that the diode D_1 conducts. If it does, we have to distinguish two cases, depending on the state of D_2. In case that D_2 is off, the voltage $u_1(t)$ only depends on $u_{0,1}(t)$, and it is easily seen from Figure 9 that

$$u_1(t) = u_{0,1}(t)/3 \quad @ \quad D_1 \textit{ on}, \text{ and } D_2 \textit{ off}. \tag{16}$$

If D_2 conducts, the voltage $u_1(t)$ is a linear superposition of $u_{1,0}(t)$ and $u_{2,0}(t)$. This is so, solely because of the presence of mutual coupling between the ports of the twoport signal generator. From Figure 9, it is also easy to find that

$$u_1(t) = \frac{3u_{0,1}(t) - u_{0,2}(t)}{8} \quad @ \quad D_1 \text{ and } D_2 \textit{ on}. \tag{17}$$

In case D_1 conducts and D_2 is off, the voltage at the second port of the twoport generator is given by $u_{0,2}(t) - u_{0,1}(t)/3$. D_2 being off, this voltage must be ≤ 0. Thus, $u_{0,1}(t) \geq 3u_{0,2}(t)$ is necessary. Moreover, since $u_1(t)$ must be ≥ 0 to make D_1 conducting, (16) requires that $u_{0,1}(t) \geq 0$. Combining both conditions, it follows that

$$D_1 \textit{ on}, \text{ and } D_2 \textit{ off} \iff u_{0,1}(t) \geq \max\left(0; 3u_{0,2}(t)\right). \tag{18}$$

When both diodes conduct, then $u_2(t) = (3u_{0,2}(t) - u_{0,1}(t))/8$, which follows from (17) and the symmetry of the circuit. Because $u_2(t)$ must be ≥ 0 in order to make D_2 conduct, it follows that $u_{0,1}(t) \leq 3u_{2,0}(t)$ must hold. Moreover, $u_1(t)$ must also be ≥ 0, so that with (17), additionally, $u_{0,1} \geq u_{0,2}/3$ must hold. Thus,

$$D_1 \text{ and } D_2 \textit{ on} \iff u_{0,2}(t)/3 \leq u_{0,1}(t) \leq 3u_{0,2}(t). \tag{19}$$

Employing (18) and (19) in (16) and (17), the voltage at the *input* of the first LPF is given by:

$$u_1(t) = \begin{cases} \dfrac{3u_{0,1}(t) - u_{0,2}(t)}{8}, & \dfrac{u_{0,2}(t)}{3} \leq u_{0,1}(t) \leq 3u_{0,2}(t), \\ u_{0,1}(t)/3, & u_{0,1}(t) \geq \max\left(0; 3u_{0,2}(t)\right), \\ 0, & \text{else.} \end{cases} \tag{20}$$

This result is shown graphically in Figure 10. Besides the three regions of the $u_{0,1}(t)$-$u_{0,2}(t)$ plane, which correspond to the three different formulas for $u_1(t)$ in (20), Figure 10 also shows the sets of points which result from $u_{0,1}(t)$ and $u_{2,0}(t)$ obeying (15), for two different values of the phase difference, φ. Note that these sets of points have elliptical shapes, with eccentricities and tilt angles depending on φ. This is the reason why the *mean* value of $u_1(t)$ depends on φ, and thus, is directly observable even *after* the low-pass filter. Its dependence on φ is shown in Figure 11. Thus, the carrier phase leaves its footstep in the mean value of the demodulated signal. With dedicated signal processing, this could be used to obtain infor-

ISBN 978-3-8007-3584-6

mation about direction of arrival and allow for spatial processing. However, such signal processing yet has to be developed.

VI. Conclusion

Antenna-coupled nanowire thermocouples are proposed as infrared detectors, which work by heating of a nanowire junction by the radiation-induced antenna currents. The resulting thermoelectric voltage, due to the Seebeck effect, constitutes the output of a square law detector which is shown to operate extremely fast. Arrays of such nano-antennas were manufactured cost-efficiently and were subject to extensive measurement. While the square law type of detection seems to restrict application of such nano-antenna arrays for wireless communications to the subset of non-coherent (and non-linear) processing, it turns out that information about the carrier phase could be obtained despite the square law detection. This opens the possibility for coherent demodulation and to all kinds of advanced spatial signal processing. Such phase recovery builds on mutual antenna coupling and requires that the square law detector acts back on the antennas. The fulfillment of the latter is not clear yet and subject to further investigations.

References

[1] G. Moddel and S. Grover, *Rectenna Solar Cells*. Springer, 2013.

[2] R. Rehm, M. Walther, J. Schmitz, F. Rutz, A. Wörl, R. Scheibner, and J. Ziegler, "Type-II Superlattices: the Fraunhofer Perspective," in *Proc. SPIE 7660, 76601G*, 2010, pp. 1–12.

[3] A. Goss, "The Pyroelectric Vidicon – A Review," in *Proc. SPIE 807, 76601G*, 1987, pp. 25–32.

[4] P. Russer, N. Fichtner, P. Lugli, W. Porod, J. A. Russer, and H. Yordanov, "Nanoelectronics-Based Integrated Antennas," *IEEE Microwave Magazine*, vol. 11, no. 7, pp. 58–71, Dec. 2010.

[5] M. Bareiß, M. Imtaar, B. Fabel, G. Scarpa, and P. Lugli, "Temperature Enhanced Large Area Nano Transfer Printing on Si/SiO_2 Substrates Using Si Wafer Stamps," *J. Adhes.*, vol. 87, no. 9, pp. 893–901, 2011.

[6] M. Bareiss, P. Krenz, G. Szakmany, B. Tiwari, D. Kaelblein, A. Orlov, G. Bernstein, G. Scarpa, B. Fabel, U. Zschieschang, H. Klauk, W. Porod, and P. Lugli, "Rectennas Revisited," *IEEE Trans. on Nanotechnology*, vol. 12, no. 6, 2013.

[7] G. Szakmany, "Antenna-Coupled Nanowire Thermocouple for Infrared Detection," *PhD. Thesis, University of Notre Dame*, 2013.

[8] F. González and G. D. Boreman, "Comparison of Dipole, Bowtie, Spiral and Log-periodic IR Antennas," *Infrared Phys. Technol.*, vol. 46, no. 5, pp. 418–428, 2005.

[9] L. Novotny, "Effective Wavelength Scaling for Optical Antennas," *Phys. Rev. Lett.*, vol. 98, no. 26, pp. 266 802–1–266 802–4, 2007.

[10] B. Slovick, J. Bean, and G. Boreman, "Angular Resolution Improvement of Infrared Phased-array Antennas," *IEEE Antenn. Wireless Propag. Lett.*, vol. 10, no. 2, pp. 119–122, 2011.

[11] P. Krenz, B. Tiwari, G. Szakmany, A. Orlov, F. González, G. Boreman, and W. Porod, "Response Increase of IR Antenna-coupled Thermocouple using Impedance Matching," *IEEE J. Quantum Electron.*, vol. 48, no. 5, pp. 659–664, 2012.

[12] G. Szakmany, P. Krenz, A. Orlov, G. Bernstein, and W. Porod, "Antenna-Coupled Nanowire Thermocouples for Infrared Detection," *IEEE Trans. on Nanotechnology*, vol. 12, no. 2, pp. 163–167, 2013.

[13] A. Balanis, *Antenna Theory*. Second Edition, John Wiley & Sons, 1997.

[14] G. Wedler and G. Alshorachi, "The Influence of Thickness on the Resistivity, the Temperature Coefficient of Resistivity and the Thermoelectric Power of Evaporated Palladium Films at 77 K and 273 K," *Think Solid Films*, vol. 74, no. 1, pp. 1–16, 1980.

[15] S. Shivaprasad and M. Angadi, "Temperature Coefficient of Resistance of Thin Palladium Films," *J. Phys. D: Appl. Phys.*, vol. 13, no. 19, pp. L171–L172, 1980.

[16] J. M. Ziman, *Principles of the Theory of Solids*, 2nd ed. Cambridge University Press, 1965.

[17] P. N. Butcher, "Thermal and Electrical Transport Formalism for Electronic Microstructures with Many Terminals," *Journal of Physics: Condensed Matter*, vol. 2, no. 22, p. 4869, Jun. 1990. [Online]. Available: http://iopscience.iop.org/0953-8984/2/22/008

[18] E. Pop, S. Sinha, and K. E. Goodson, "Heat Generation and Transport in Nanometer-scale Transistors," *Proceedings of the IEEE*, vol. 94, no. 8, pp. 1587–1601, 2006.

[19] A. Raman, D. G. Walker, and T. S. Fisher, "Simulation of Non-Equilibrium Thermal Effects in Power LDMOS Transistors," *Solid-State Electronics*, vol. 47, no. 8, pp. 1265–1273, Aug. 2003.

[20] N. F. Mott and H. Jones, *The Theory of the Properties of Metals and Alloys*. London: Oxford University Press, 1936.

[21] F. L. Bakker, J. Flipse, and B. van Wees, "Nanoscale Temperature Sensing using the Seebeck Effect," *Journal of Applied Physics*, vol. 111, no. 8, pp. 084 306–084 306–4, 2012.

[22] E.-S. Lee, S. Cho, H.-K. Lyeo, and Y.-H. Kim, "Evaluating the Seebeck Effect at the Atomic Scale," arXiv e-print 1307.3742, Jul. 2013. [Online]. Available: http://arxiv.org/abs/1307.3742

[23] M. N. Ozisik, *Boundary Value Problems of Heat Conduction*. Courier Dover Publications, 2002.

[24] R. Hull, *Properties of Crystalline Silicon*, ser. Electronic Materials Information Service: EMIS datareviews series ; 20. London: INSPEC, 1999.

[25] P. Russer, J. A. Russer, F. Mukhtar, P. Lugli, S. Wane, D. Bajon, and W. Porod, "Integrated Antennas for RF Sensing, Wireless Communications and Energy Harvesting Applications," in *International Workshop on Antenna Technology, iWAT 2013*, Karlsruhe, March 4-6 2013.

[26] J. Russer, F. Mukhtar, S. Wane, D. Bajon, and P. Russer, "Network Model of Coupled Integrated Antennas," in *Proc. of 2013 International Conference on Electromagnetics in Adcanced Applications (ICEAA)*, 2013, pp. 956–959.

[27] S. A. Maas, *Nonlinear Microwave and RF Circuits*. Boston: Artech House, 2003.

[28] M. Haardt, *Efficient One-, Two-, and Multidimensional High-Resolution Array Signal Processing*. Aachen, Germany: Shaker Verlag, 1996.

[29] R.-U. Choi and R. Murch, "A Transmit Preprocessing Technique for Multiuser MIMO Systems using a Decomposition Approach," *IEEE Transactions on Wireless Communications*, vol. 3, no. 1, pp. 20–23, 2004.

[30] M.T. Ivrlač and J.A. Nossek, "Toward a Circuit Theory of Communication," *IEEE Transactions on Circuits and Systems I: Regular Papers*, vol. 57(7), pp. 1663–1683, 2010.

[31] J. S. Hammerschmidt and C. Brunner, "The Implications of Array and Multipath Geometries in Spatial Processing," in *Proc. IEEE/IEE Int. Conf. on Telecommunications*, Acapuloco, Mexico, May 2000.

[32] M.T. Ivrlač and J.A. Nossek, "On Multistreaming with Compact Antenna Arrays," in *Proc. of the 30 th. General Assembly of the URSI*, Istanbul, Turkey, 2011.

[33] I. E. Telatar, "Capacity of Multi-Antenna Gaussian Channels," *European Transactions on Telecommunications*, vol. 10(6), pp. 585–596, nov 1999.

[34] M.T. Ivrlač and J.A. Nossek, "On Multistreaming with Compact Antenna Arrays," in *Proc. of 2011 International ITG Workshop on Smart Antennas (WSA)*, 2011, pp. 1–8.

[35] F. Stremler, *Communication Systems*. Addison Wesley, 1990.

ISBN 978-3-8007-3584-6